





Article

Development of $\text{Na}_{0.5}\text{CoO}_2$ Thick Film Prepared by Screen-Printing Process

Akihiro Tsuruta ^{1,*}, Miki Tanaka ¹, Masashi Mikami ¹, Yoshiaki Kinemuchi ¹,
Yoshitake Masuda ¹, Woosuck Shin ¹ and Ichiro Terasaki ^{1,2}

¹ National Institute of Advanced Industrial Science and Technology (AIST), Shimo-Shidami, Moriyama-ku, Nagoya 463-8560, Japan; tanaka.miki@aist.go.jp (M.T.); m-mikami@aist.go.jp (M.M.); y.kinemuchi@aist.go.jp (Y.K.); masuda-y@aist.go.jp (Y.M.); w.shin@aist.go.jp (W.S.)

² Department of Physics, Nagoya University, Furo-cho, Chikusa-ku, Nagoya 464-8602, Japan; terra@nagoya-u.jp

* Correspondence: a.tsuruta@aist.go.jp; Tel.: +81-52-736-7481

Received: 26 May 2020; Accepted: 18 June 2020; Published: 22 June 2020



Abstract: The $\text{Na}_{0.5}\text{Co}_{0.9}\text{Cu}_{0.1}\text{O}_2$ thick film with the same thermoelectric performance as a $\text{Na}_{0.5}\text{CoO}_2$ bulk was formed on an alumina substrate by the screen-printing process. The power factor exceeded $0.3 \text{ mW/K}^2\text{m}$, with the resistivity of $3.8 \text{ m}\Omega\text{cm}$ and the thermopower of $108 \mu\text{V/K}$. The thick film without any cracks strongly adhered to the substrate. The high-quality thick film had been realized through the carefully designed and improved process, mixing NaCl to promote the anisotropic sintering of $\text{Na}_{0.5}\text{Co}_{0.9}\text{Cu}_{0.1}\text{O}_2$, inserting a CuO interlayer to adhere the film and substrate, and Co–Cu substituting Cu for Co to control the sintering temperature.

Keywords: screen print; sodium cobaltite; thermoelectric; thick film

1. Introduction

Thermoelectric (TE) materials can convert heat energy directly into electrical energy without any moving parts or emitting environmental pollutants. This clean power generation is expected to be a technology that can effectively utilize the waste heat from other power generations as well as various devices, because TE can generate power even from a small amount of thermal energy that cannot turn the turbine. In order to enhance the conversion efficiency, various inorganic materials, such as the Bi–Te system [1–3], SnSe [4,5], and Heusler compounds [6–8], have been studied steadily for a long time. Recently, flexible and/or wearable devices contributing to IoT have attracted attention, even in the field of thermoelectricity [9], and organic thermoelectric materials such as PEDOT:PSS (Poly(3,4-ethylenedioxythiophene):Poly(styrenesulfonate)) are also being actively studied [10].

Harvesting diluted waste heat requires a module design that can concentrate a heat flow into TE materials, and a planar TE device is one of the ways [11,12]. Such a TE device could potentially replace the battery in IoT devices which need a power of several mW, otherwise the battery should be replaced every month. Furthermore, the planar-shaped device realized by the printing process could be freely designed in size and shape, and would be able to propose an appropriate design for various heat sources. A screen-printing process is the most popular and traditional of the various printing processes, because the low process cost and high productivity are suitable for industrial applications. The process has long been used for conductive circuit patterning, and many pastes for metal thick films are commercially available. Even today, the processes and pastes are investigated to realize fine line patterning for the product miniaturization and integration [13,14], and the latest research has achieved printing with a width of $30 \mu\text{m}$ or less using silver paste [15]. The development of carbon-based conductive circuit printing for flexible devices is also active [16,17], but there are few

reports on ceramic material printing, with a serious problem in thick film sintering such as a cracking due to the sintering shrinkage [18,19].

We chose oxides as the thermoelectric material, favoring the high stability and low toxicity. The high thermoelectric performance of the metallic layered transition-metal oxide, $\text{Na}_{0.5}\text{CoO}_2$, as a p-type TE material had been reported by Terasaki et al. [20]. The low resistivity originates in its high carrier density, whereas the high thermopower is maintained by the orbital and spin entropies derived from the Mott insulator. The thermoelectric power factor $S^2\rho^{-1}$, where ρ is resistivity and S is thermopower, of a $\text{Na}_{0.5}\text{CoO}_2$ single crystal reaches $5 \text{ mW/K}^2\text{m}$ at 300 K in the in-plane direction [20] and exceeds $4 \text{ mW/K}^2\text{m}$ of Bi_2Te_3 [21]. Since $\text{Na}_{0.5}\text{CoO}_2$ shows anisotropic electrical conductivity and the resistivity in the out-of-plane direction is approximately 50 times higher than that in the in-plane direction, the power factor of $\text{Na}_{0.5}\text{CoO}_2$ polycrystalline sample is $0.25 \text{ mW/K}^2\text{m}$ at 300 K. However, $\text{Na}_{0.5}\text{CoO}_2$ demonstrates superior performance compared to the other oxide materials, and is a promising thermoelectric material.

In this paper, we report the thermoelectric properties and structure of developed $\text{Na}_{0.5}\text{CoO}_2$ thick film and discuss the significance of our improved process. In particular, we have introduced a sintering additive into the thick film and an interlayer between the thick film and a substrate, and further adjusted the composition of the thick film.

2. Experimental

The $\text{Na}_{0.5}\text{Co}_{0.9}\text{Cu}_{0.1}\text{O}_2$ powder was prepared by a solid-state reaction. Na_2CO_3 , Co_3O_4 , and CuO were mixed and calcined at $860 \text{ }^\circ\text{C}$ for 12 h in air. The calcined products were ground, pressed into a pellet, and sintered at $920 \text{ }^\circ\text{C}$ for 12 h in air. The $\text{Na}_{0.5}\text{Co}_{0.9}\text{Cu}_{0.1}\text{O}_2$ powder was obtained via a mechanical grinding and ball milling of the pellet. The $\text{Na}_{0.5}\text{CoO}_2$ powder was prepared by the same process from Na_2CO_3 and Co_3O_4 .

The paste for the main $\text{Na}_{0.5}\text{Co}_{0.9}\text{Cu}_{0.1}\text{O}_2$ layer was comprised of a mixture of synthesized $\text{Na}_{0.5}\text{Co}_{0.9}\text{Cu}_{0.1}\text{O}_2$ powder and ground NaCl powder, a vehicle of Terpineol and Ethyl cellulose. The volume fraction of NaCl in the mixture was optimized to 20 vol%. The paste for the CuO interlayer consisted of CuO powder and the same vehicle as that of the main layer. The pastes of $\text{Na}_{0.5}\text{CoO}_2$ without NaCl , and $\text{Na}_{0.5}\text{CoO}_2$ with 20 vol% NaCl , were also prepared by mixing the same vehicle.

The CuO paste was printed on an alumina substrate ($10 \text{ mm} \times 20 \text{ mm} \times 1 \text{ mm}$) in a rectangular shape ($10 \text{ mm} \times 2 \text{ mm}$) using a screen-printing process. The printed film was sintered at $950 \text{ }^\circ\text{C}$ for 12 h in air after drying the vehicle at $200 \text{ }^\circ\text{C}$ for 5 min. Subsequently, the NaCl -mixed $\text{Na}_{0.5}\text{Co}_{0.9}\text{Cu}_{0.1}\text{O}_2$ paste was printed on the sintered CuO interlayer in the same shape. The vehicle was dried in the same manner as mentioned. The screen printing of both layers was performed at the print speed of 50 mm/s using a stainless steel mesh screen with 250-mesh/inch by a semi-auto screen printing machine (SERIA CORPORATION, SSA-PC150E-IP, Tokyo, Japan). In order to achieve $100 \text{ }\mu\text{m}$ of the thickness after drying, the $\text{Na}_{0.5}\text{Co}_{0.9}\text{Cu}_{0.1}\text{O}_2$ paste was laminated 10 times under the same printing condition. The sintering of the dried film was carried out at $920 \text{ }^\circ\text{C}$ for 1 h in air.

In this paper, two other kinds of thick films were also prepared for comparison. One is a $\text{Na}_{0.5}\text{CoO}_2$ thick film prepared by a simple screen-printing process. Here, only the $\text{Na}_{0.5}\text{CoO}_2$ paste was printed and laminated 10 times on an alumina substrate in a rectangular shape ($10 \text{ mm} \times 5 \text{ mm}$). Another thick film was prepared by a partially improved process. The NaCl -mixed $\text{Na}_{0.5}\text{CoO}_2$ paste was printed and laminated 10 times on a CuO interlayer, which was printed and sintered on an alumina substrate in a rectangular shape ($10 \text{ mm} \times 2 \text{ mm}$). The printing, drying, and sintering conditions of both of the main layers (the $\text{Na}_{0.5}\text{CoO}_2$ layer and the NaCl -mixed $\text{Na}_{0.5}\text{CoO}_2$ layer) and the CuO interlayer were the same with those of the NaCl -mixed $\text{Na}_{0.5}\text{Co}_{0.9}\text{Cu}_{0.1}\text{O}_2$ layer and the CuO interlayer as mentioned above, respectively.

X-ray diffraction (XRD) patterns of the thick film were taken with $\text{CuK}\alpha$ radiation using a standard diffractometer with a monochromator (Rigaku SmartLab, Tokyo, Japan). The XRD measurement was performed in $2\theta/\theta$ -scan mode against the sample surface, i.e., a plane parallel to the substrate surface.

The resistivity and thermopower were measured by the four-point probe method and EMFs under temperature gradients using Pt thermocouples, respectively, in air from 50 °C to 550 °C (Ozawa Science RZ2001S, Nagoya, Japan). The morphology and element mapping of the thick film were observed using a scanning electron microscope (SEM; JEOL, JSM-5600, Tokyo, Japan) and energy-dispersive X-ray spectrometry (EDX; JEOL, EX-54145JMU, Tokyo, Japan). The thermal behaviors of the $\text{Na}_{0.5}\text{CoO}_2$ and $\text{Na}_{0.5}\text{Co}_{0.9}\text{Cu}_{0.1}\text{O}_2$ powders were analyzed by a thermogravimetry and differential thermal analyzer (TG/DTA; BRUKER, MTC1000SA, Billerica, MA, USA) from 15 °C to 950 °C in air.

3. Results and Discussion

3.1. Problems with a Thick Film Prepared by a Simple Printing Process

As a first approach to forming a $\text{Na}_{0.5}\text{CoO}_2$ thick film, we simply screen-printed and sintered the $\text{Na}_{0.5}\text{CoO}_2$ paste on an alumina substrate. Figure 1a,b show a cross-sectional schematic of a printed thick film, and photographs of a dried and a sintered thick film prepared by the simple screen-printing process, respectively. The thick film was cracked severely after sintering and easily peeled from the substrate. In addition, $\text{Na}_{0.5}\text{CoO}_2$ has decomposed to Co_3O_4 due to the evaporation of Na during sintering, as shown in Figure 1c.

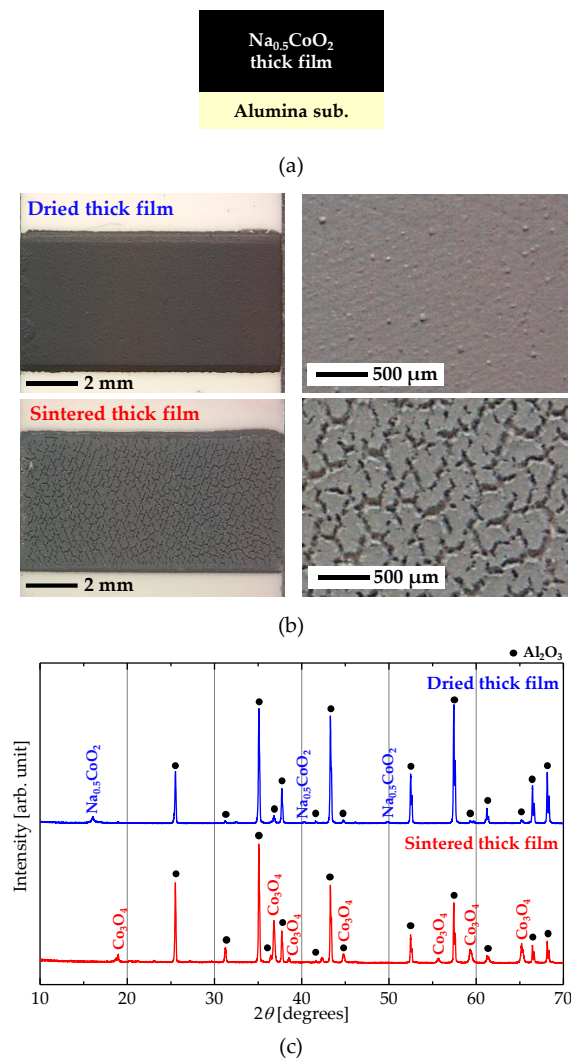


Figure 1. (a) Cross-sectional schematic of a printed $\text{Na}_{0.5}\text{CoO}_2$ thick film on an alumina substrate as a first approach. (b) Photographs and (c) XRD ($\text{CuK}\alpha$) patterns of a dried and a sintered $\text{Na}_{0.5}\text{CoO}_2$ thick film prepared by the simple screen-printing process.

In order to suppress the evaporation of Na, we employed flux sintering using NaCl. Furthermore, the interface between the film and substrate was modified by an insertion of a CuO interlayer in order to improve the adhesion strength. The cross-sectional schematic and the photograph of a partially improved $\text{Na}_{0.5}\text{CoO}_2$ thick film with NaCl mixing and a CuO interlayer introduction are shown in Figure 2a,b, respectively. NaCl mixing drastically changes the appearance of the film to be free of cracks, and more importantly, the decomposition was totally prevented. As expected, the CuO interlayer introduction improved the adhesion strength and prevented the peeling of the thick film.

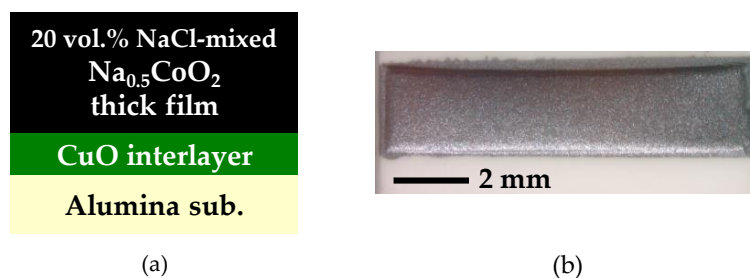


Figure 2. (a) Cross-sectional schematic and (b) photograph of a partially improved $\text{Na}_{0.5}\text{CoO}_2$ thick film with NaCl mixing and a CuO interlayer introduction.

However, bending and arching of the film on the CuO interlayer were found due to the sintering shrinkage. Through several attempts, we found that Cu substitution into Co site prevent the delamination. TG/DTA analysis revealed the difference in the stability between $\text{Na}_{0.5}\text{CoO}_2$ and $\text{Na}_{0.5}\text{Co}_{0.9}\text{Cu}_{0.1}\text{O}_2$ as shown in Figure 3. The weight loss was significantly reduced by the substitution. In addition to that, a faint endothermic peak at 890 °C shifted to 830 °C. K. Park et al. has reported that this Co–Cu substitution reduces the melting temperature of $\text{Na}_{0.5}\text{CoO}_2$ [22]. Although the observed peaks are much lower than the melting point, the shift indicates the reduced temperature stability by the substitution as well. In other words, $\text{Na}_{0.5}\text{Co}_{0.9}\text{Cu}_{0.1}\text{O}_2$ is more reactive than $\text{Na}_{0.5}\text{CoO}_2$, which is beneficial to improve sintering. As a result, well-adhered thick film without any cracks was attained as shown later.

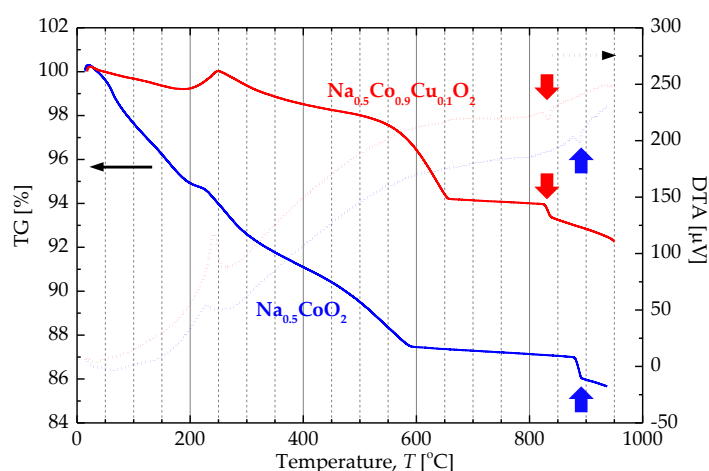


Figure 3. Thermogravimetry/differential thermal analyzer (TG/DTA) curves of $\text{Na}_{0.5}\text{CoO}_2$ and $\text{Na}_{0.5}\text{Co}_{0.9}\text{Cu}_{0.1}\text{O}_2$ powders.

3.2. Microstructure of Crack-Free Thick Film

Figure 4a shows the cross-sectional schematic of the $\text{Na}_{0.5}\text{Co}_{0.9}\text{Cu}_{0.1}\text{O}_2$ thick film prepared by the improved process. Compared to the partially improved thick film shown in Figure 2a, the composition of the main layer had been changed from $\text{Na}_{0.5}\text{CoO}_2$ to $\text{Na}_{0.5}\text{Co}_{0.9}\text{Cu}_{0.1}\text{O}_2$. Figure 4(b1) shows a photograph of the entire $\text{Na}_{0.5}\text{Co}_{0.9}\text{Cu}_{0.1}\text{O}_2$ thick film, and Figure 4(b2) shows an enlarged portion

of the area surrounded by the red broken line in Figure 4(b1). The thick film has a glossy surface, indicating a finely sintered dense film. No cracks can be seen with an optical microscope. In addition, the thick film is strongly adhered to an alumina substrate and passed the adhesive tape peeling test. This appearance fully satisfies the requirements for a thick film structure and is expected to perform well.

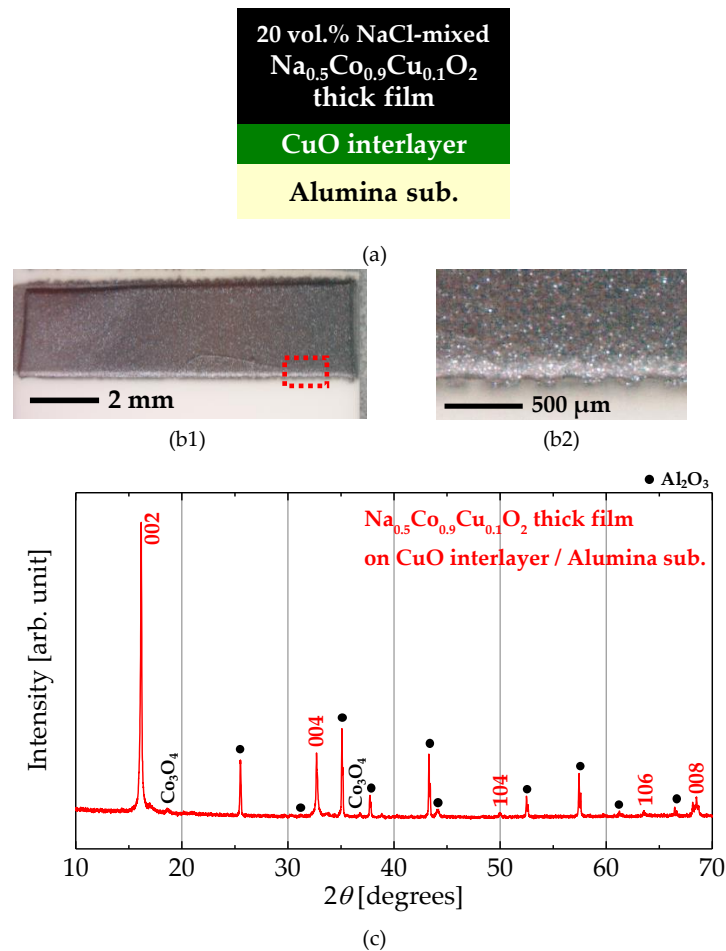


Figure 4. (a) Cross-sectional schematic of a $\text{Na}_{0.5}\text{Co}_{0.9}\text{Cu}_{0.1}\text{O}_2$ thick film prepared by the improved process. (b1,b2) Photographs of the $\text{Na}_{0.5}\text{Co}_{0.9}\text{Cu}_{0.1}\text{O}_2$ thick film; (b1) shows the entire film and (b2) shows an enlarged portion surrounded by a red broken line in (b1). (c) The XRD ($\text{CuK}\alpha$) pattern of the $\text{Na}_{0.5}\text{Co}_{0.9}\text{Cu}_{0.1}\text{O}_2$ thick film. The peaks with Miller indices correspond to $\text{Na}_{0.5}\text{CoO}_2$ phase.

Figure 4c shows the XRD pattern of the $\text{Na}_{0.5}\text{Co}_{0.9}\text{Cu}_{0.1}\text{O}_2$ thick film. The indexed peaks correspond to the $\text{Na}_{0.5}\text{CoO}_2$ phase. Co_3O_4 , which is thought to have been formed by the decomposition of a small amount of $\text{Na}_{0.5}\text{Co}_{0.9}\text{Cu}_{0.1}\text{O}_2$ by the evaporation of Na, is confirmed as an impurity. It should be noted that the $\text{Na}_{0.5}\text{CoO}_2$ phase, which was completely degraded in the trial sample, remained mostly in the improved thick film. Since the sintering temperature and atmosphere of the films were exactly the same, the decomposition of the $\text{Na}_{0.5}\text{CoO}_2$ phase was suppressed by the Na-rich surroundings with mixed NaCl. The peaks corresponding to the (00n) planes of the $\text{Na}_{0.5}\text{CoO}_2$ phase are stronger than the other peaks compared to reported powder diffraction patterns. Namely, the c-axis of the $\text{Na}_{0.5}\text{CoO}_2$ phase is oriented perpendicular to the substrate, at least near the film surface where the X-ray can penetrate. The c-axis length, calculated from the 00n peaks, are 10.95 Å, and it corresponds to the Na-rich composition of $\text{Na}_{0.68}\text{CoO}_2$ in comparison with data reported by Shu et al. [23]. The excess Na, induced from NaCl, has been intercalated into $\text{Na}_{0.5}\text{Co}_{0.9}\text{Cu}_{0.1}\text{O}_2$. Although the Co–Cu substitution should change the axis length, the effect on the c-axis should be slight

since the ionic radii of Co and Cu are similar. Certainly, the $00n$ peak shift with the Co–Cu substitution has been invisible in the previous report [22,24].

The cross-sectional SEM observation image of the $\text{Na}_{0.5}\text{Co}_{0.9}\text{Cu}_{0.1}\text{O}_2$ thick film is shown in Figure 5(a1). The well-sintered CuO interlayer with a thickness of approximately $15\ \mu\text{m}$ is clearly observed on the alumina substrate, on which the $\text{Na}_{0.5}\text{Co}_{0.9}\text{Cu}_{0.1}\text{O}_2$ layer with a thickness of $50\ \mu\text{m}$ is laminated. No cracks can be observed, and all layers are firmly adhered. It is noteworthy that the $\text{Na}_{0.5}\text{Co}_{0.9}\text{Cu}_{0.1}\text{O}_2$ layer clearly separates a $30\ \mu\text{m}$ -thick plate-crystal layer from the surface and a $20\ \mu\text{m}$ -thick isotropic-crystal layer near the CuO interlayer. Figure 5(a2) shows an enlarged image of the interface between the layers. So far, preferential growth of $\text{Na}_{0.5}\text{CoO}_2$ has been reported in the templated grain growth process using NaCl flux [25] as well as hot-forged sintering [26], leading to the well-aligned microstructure along the ab -plane. In our $\text{Na}_{0.5}\text{Co}_{0.9}\text{Cu}_{0.1}\text{O}_2$ thick film, the mixed NaCl would have acted as a flux that promotes the crystal growth of $\text{Na}_{0.5}\text{Co}_{0.9}\text{Cu}_{0.1}\text{O}_2$. This leads to the growth of plate-crystals, reflecting its layered crystal structure and crystal orientation along with the interface. Typically, cracks in printed thick films are caused by the mismatch between the sintering shrinkage of the film and in-plane constraint from the substrate. Then, brittle ceramic materials are hard to sinter into crack-free thick films (compared to metallic materials that can deform). On the contrary, in our flux sintered thick film, the crystals grew in the in-plane direction of the film, supporting the anisotropic sintering of the film in such a way that effectively suppressed crack formation. Notably, with both the layered crystal structure of $\text{Na}_{0.5}\text{Co}_{0.9}\text{Cu}_{0.1}\text{O}_2$ and the crystal growth with NaCl flux, the isotropic crystal growth of $\text{Na}_{0.5}\text{Co}_{0.9}\text{Cu}_{0.1}\text{O}_2$ just above the CuO interlayer is rather unnatural.

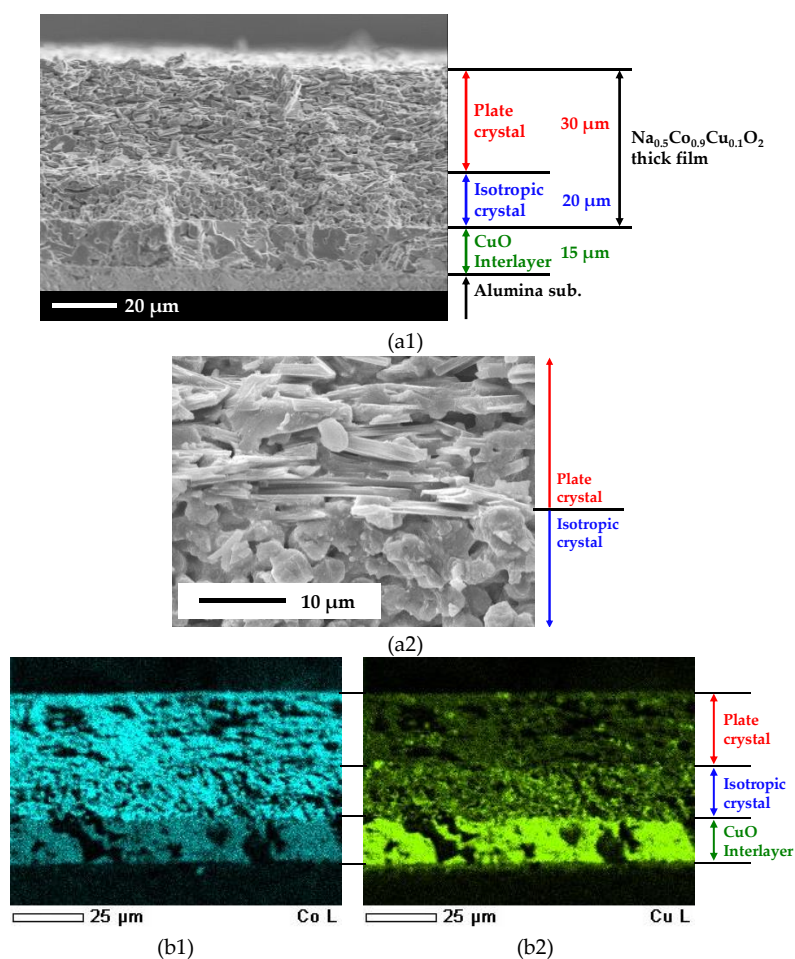


Figure 5. (a1) Cross-sectional SEM image of the $\text{Na}_{0.5}\text{Co}_{0.9}\text{Cu}_{0.1}\text{O}_2$ thick film. (a2) An enlarged image of the interface between the plate-crystal layer and the isotropic-crystal layer. (b1,b2) Element mapping images of the $\text{Na}_{0.5}\text{Co}_{0.9}\text{Cu}_{0.1}\text{O}_2$ thick film for (b1) Co and (b2) Cu.

Figure 5(b1,b2) show the cross-sectional element mapping images of the $\text{Na}_{0.5}\text{Co}_{0.9}\text{Cu}_{0.1}\text{O}_2$ thick film for Co and Cu, respectively. In the plate-crystal layer, Co and Cu coexist, and both are uniformly distributed throughout the layer, indicating that Cu substitutes to Co site in $\text{Na}_{0.5}\text{CoO}_2$. On the other hand, in the isotropic-crystal layer, Co is uniformly distributed throughout the layer just as with the plate-crystal layer, but the Cu distribution has a distinct gradation. The high brightness of Cu concentration in the isotropic-crystal layer is approximately the same with the CuO interlayer, suggesting the presence of Cu-rich impurities. Co is also found in the CuO interlayer. Co can substitute Cu site in CuO, thus Co ions would diffuse into the CuO interlayer during the sintering, and NaCl flux would promote the diffusion.

In order to identify the compounds contained in each layer, the thick film was polished from the surface, and each exposed layer was measured by XRD. Figure 6 shows XRD patterns of each layer. The indexed peaks and the unassigned peaks correspond to the $\text{Na}_{0.5}\text{CoO}_2$ phase and alumina substrate, respectively. The peaks of the $\text{Na}_{0.5}\text{CoO}_2$ phase are located at the same angle in all layers. There are peaks of CuO in addition to the peaks of the $\text{Na}_{0.5}\text{CoO}_2$ phase in the isotropic-crystal layer, and Co_3O_4 observed in the plate-crystal layer. Hence, the Cu-rich impurity observed in the elemental mapping image is CuO, and the isotropic-crystal layer is a composite of $\text{Na}_{0.5}\text{Co}_{0.9}\text{Cu}_{0.1}\text{O}_2$, Co_3O_4 , and CuO. CuO forms large grains because Cu-rich grains are relatively large in the mapping image. Such CuO with a $C12/c1$ space group of monoclinic should form isotropic grains and may act as a grain growth inhibitor for $\text{Na}_{0.5}\text{Co}_{0.9}\text{Cu}_{0.1}\text{O}_2$, resulting in the isotropic $\text{Na}_{0.5}\text{Co}_{0.9}\text{Cu}_{0.1}\text{O}_2$ crystals. The origin of Cu-source that form CuO grains should be the CuO interlayer exuded as a liquid phase or dissolved in NaCl flux, since the Cu concentration in $\text{Na}_{0.5}\text{Co}_{0.9}\text{Cu}_{0.1}\text{O}_2$ is much lower than that of CuO. Co in the CuO interlayer formed Co_3O_4 .

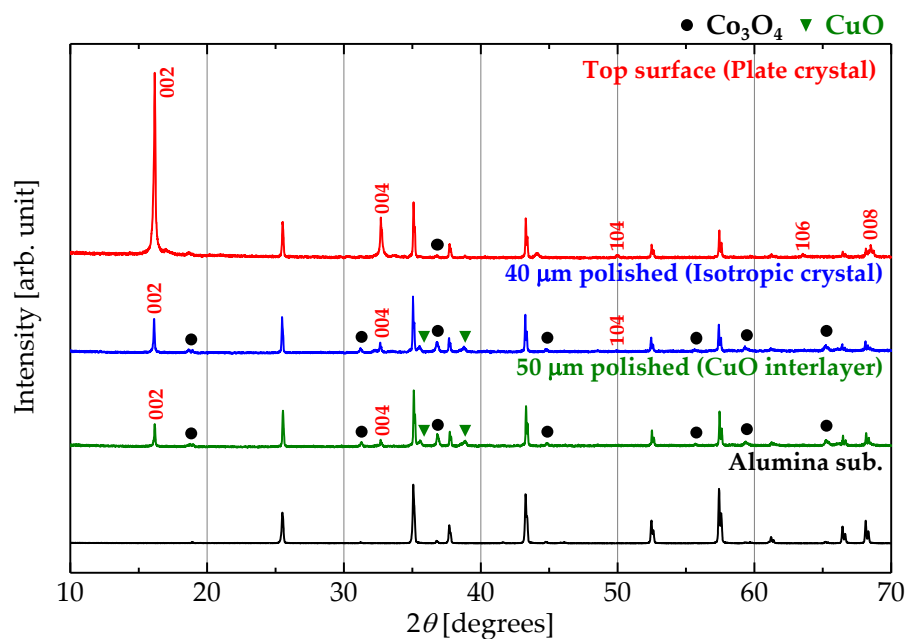


Figure 6. XRD ($\text{CuK}\alpha$) patterns of the plate-crystal layer, the isotropic crystal layer, the CuO interlayer, and the alumina substrate in the $\text{Na}_{0.5}\text{Co}_{0.9}\text{Cu}_{0.1}\text{O}_2$ thick film. Each layer was exposed by polishing from the surface of the film.

CuO has been sintered in a liquid phase at an interlayer sintering temperature of $950\text{ }^\circ\text{C}$, and penetrated into a $\text{Na}_{0.5}\text{Co}_{0.9}\text{Cu}_{0.1}\text{O}_2$ layer with NaCl flux. Therefore, the CuO interlayer adheres to both of the alumina substrate and the $\text{Na}_{0.5}\text{Co}_{0.9}\text{Cu}_{0.1}\text{O}_2$ thick film by the anchor effect, and adheres the thick film to the substrate strongly. In addition, CuO is compatible with alumina substrates from the viewpoint of thermal expansion [27,28].

3.3. Thermoelectric Properties of $\text{Na}_{0.5}\text{Co}_{0.9}\text{Cu}_{0.1}\text{O}_2$ Thick Film

Figure 7 shows the temperature (T), dependence of resistivity (ρ), thermopower (S), and power factor ($S^2\rho^{-1}$) of a $\text{Na}_{0.5}\text{CoO}_2$ bulk, a $\text{Na}_{0.5}\text{Co}_{0.9}\text{Cu}_{0.1}\text{O}_2$ bulk, and the $\text{Na}_{0.5}\text{Co}_{0.9}\text{Cu}_{0.1}\text{O}_2$ thick film. The $\text{Na}_{0.5}\text{CoO}_2$ bulk showed similar thermoelectric properties with various reported polycrystalline samples. On the other hand, although the thermopower of our $\text{Na}_{0.5}\text{Co}_{0.9}\text{Cu}_{0.1}\text{O}_2$ bulk was a similar value to the $\text{Na}_{0.5}\text{Co}_{0.9}\text{Cu}_{0.1}\text{O}_2$ bulk reported by Terasaki et al. [29], the resistivity was more than twice the reported values [22,29]. The cause of the high resistivity of the bulk should be its low density due to non-optimized process. The $\text{Na}_{0.5}\text{Co}_{0.9}\text{Cu}_{0.1}\text{O}_2$ thick film shows lower resistivity than our $\text{Na}_{0.5}\text{CoO}_2$ bulk and the reported $\text{Na}_{0.5}\text{Co}_{0.9}\text{Cu}_{0.1}\text{O}_2$ bulk at all temperatures. It has been reported that the resistivity in the in-plane direction is one order of magnitude lower than the resistivity in the out-of-plane direction [20]. Co–Cu substitution and Na content in $\text{Na}_{0.5}\text{CoO}_2$ also have an influence on resistivity, because both change the carrier density through reducing the amount, or changing the valence, of Co. However, the change in resistivity caused by the factor related to composition is smaller than that caused by the anisotropy. Hence the preferred orientation of ab -plane is responsible for the low resistivity. Certainly, the textured $\text{Na}_{0.5}\text{CoO}_2$ ceramics, with the well aligned ab -plane prepared by the reactive templated grain growth (RTGG) method [30], show lowest resistivity in Figure 7a.

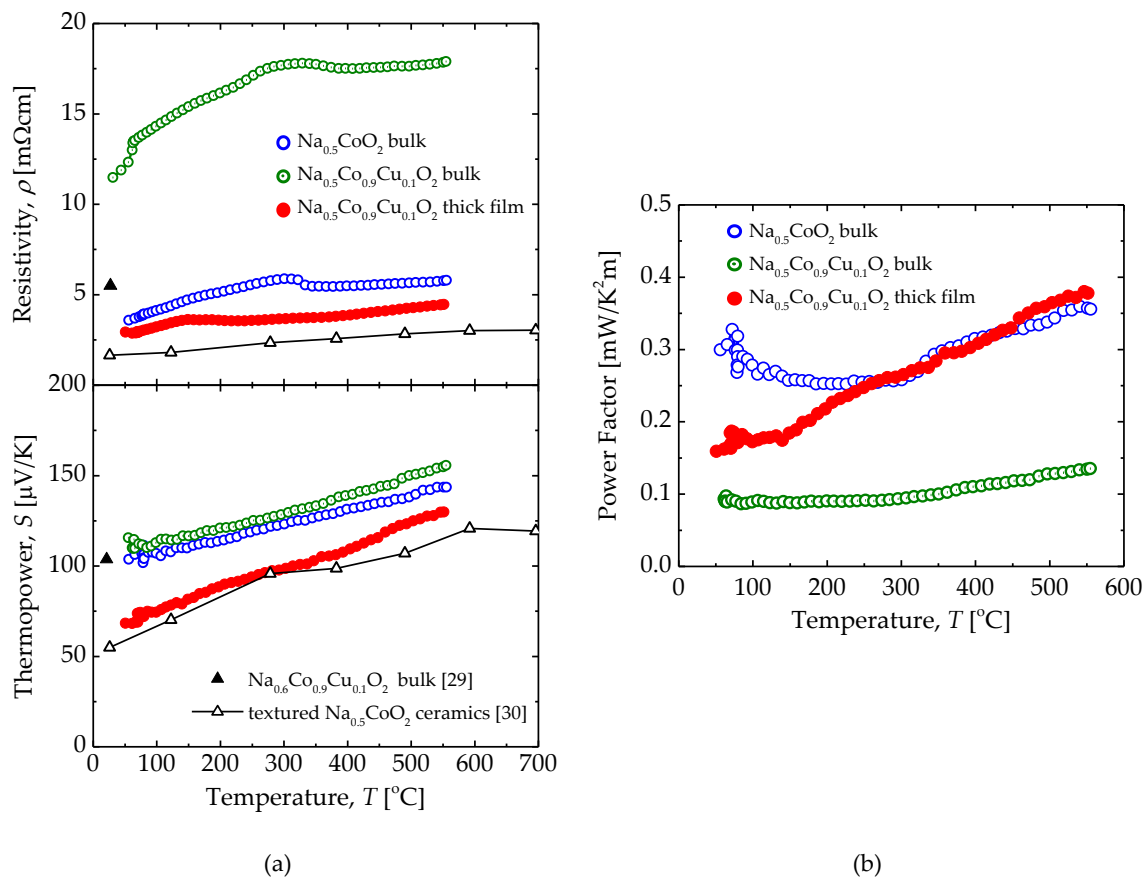


Figure 7. Temperature dependence of (a) resistivity, thermopower, and (b) power factor for a $\text{Na}_{0.5}\text{CoO}_2$ bulk, a $\text{Na}_{0.5}\text{Co}_{0.9}\text{Cu}_{0.1}\text{O}_2$ bulk, and the $\text{Na}_{0.5}\text{Co}_{0.9}\text{Cu}_{0.1}\text{O}_2$ thick film measured in air.

The thermopower of the $\text{Na}_{0.5}\text{Co}_{0.9}\text{Cu}_{0.1}\text{O}_2$ thick film was lower than that of the bulk samples. The thermopower has been reported to be enhanced by a Co–Cu substitution in $\text{Na}_{0.5}\text{CoO}_2$, and increased with increasing Na content in a previous study [29,31]. As shown in Figure 7a, $\text{Na}_{0.5}\text{Co}_{0.9}\text{Cu}_{0.1}\text{O}_2$ bulk shows higher thermopower than the $\text{Na}_{0.5}\text{CoO}_2$ bulk. The thermopower of the $\text{Na}_{0.5}\text{Co}_{0.9}\text{Cu}_{0.1}\text{O}_2$ bulk reported by Park et al. has exceeded 400 $\mu\text{V}/\text{K}$ at 600 $^{\circ}\text{C}$ [22], and it is much higher than the other reports and the theoretical value calculated from the Heikes formula

with the valence ratio of $\text{Co}^{3+}:\text{Co}^{4+} = 1:1$ [32,33], but the reason for this is not clear. Nevertheless, the $\text{Na}_{0.5}\text{Co}_{0.9}\text{Cu}_{0.1}\text{O}_2$ thick film, which is expected to be a Na-rich composition with Co–Cu substitution, shows lower thermopower than the $\text{Na}_{0.5}\text{CoO}_2$ bulk.

In careful consideration for thermopower reduction, such a low value can only be attributed to the Na-poor composition in the outermost surface of the thick film. Na reduction leads to the increase of the Co^{4+} ratio in Co ions and reduces thermopower, theoretically [34]. A similar unexplained reduction in the thermopower has also been observed in the textured $\text{Na}_{0.5}\text{CoO}_2$ ceramics prepared by RTGG method. The thermopower of the $\text{Na}_{0.5}\text{CoO}_2$ ceramics and the $\text{Na}_{0.5}\text{Co}_{0.9}\text{Cu}_{0.1}\text{O}_2$ thick film are in very good agreement. Both have the common features that they are polycrystals with a well aligned *ab*-plane and both have been sintered in a thin form with a large surface area. In both cases, the large surface area might be the cause of the Na-poor composition and thermopower reduction in the outermost surface.

As a result, the $\text{Na}_{0.5}\text{Co}_{0.9}\text{Cu}_{0.1}\text{O}_2$ thick film with superior resistivity and inferior thermopower to the $\text{Na}_{0.5}\text{CoO}_2$ bulk shows a comparable power factor with $\text{Na}_{0.5}\text{CoO}_2$ bulk as shown in Figure 7b.

4. Conclusions

We fabricated a $\text{Na}_{0.5}\text{Co}_{0.9}\text{Cu}_{0.1}\text{O}_2$ thick film with the same thermoelectric performance as a $\text{Na}_{0.5}\text{CoO}_2$ bulk on an alumina substrate by screen-printing process. The thick film had no cracks and adhered to the substrate strongly. Mixing NaCl flux into the $\text{Na}_{0.5}\text{Co}_{0.9}\text{Cu}_{0.1}\text{O}_2$ thick film promoted the sintering of $\text{Na}_{0.5}\text{Co}_{0.9}\text{Cu}_{0.1}\text{O}_2$ and the formation of plate-crystals according to the anisotropic crystal structure of the $\text{Na}_{0.5}\text{CoO}_2$ system. The cracks, which should be formed through the sintering shrinkage, were suppressed via the anisotropic sintering of the thick film caused by the growth and in-plane alignment of the plate $\text{Na}_{0.5}\text{Co}_{0.9}\text{Cu}_{0.1}\text{O}_2$ crystals. In the $\text{Na}_{0.5}\text{Co}_{0.9}\text{Cu}_{0.1}\text{O}_2$ thick film, there was an isotropic $\text{Na}_{0.5}\text{Co}_{0.9}\text{Cu}_{0.1}\text{O}_2$ crystals layer just on the CuO interlayer. CuO inhibited the crystal growth of $\text{Na}_{0.5}\text{Co}_{0.9}\text{Cu}_{0.1}\text{O}_2$ and made $\text{Na}_{0.5}\text{Co}_{0.9}\text{Cu}_{0.1}\text{O}_2$ to form isotropic crystals, while providing strong adhesion to the substrate. The *ab*-plane alignment of $\text{Na}_{0.5}\text{Co}_{0.9}\text{Cu}_{0.1}\text{O}_2$ reduced the resistivity of the thick film compared with a $\text{Na}_{0.5}\text{CoO}_2$ bulk. The thick film showed smaller thermopower than a $\text{Na}_{0.5}\text{CoO}_2$ bulk. The reason for the thermopower reduction would be Na-poor composition at the outermost surface, and the value and temperature dependence were in very good agreement with the reported $\text{Na}_{0.5}\text{CoO}_2$ ceramics with a similar structure. As a result, the $\text{Na}_{0.5}\text{Co}_{0.9}\text{Cu}_{0.1}\text{O}_2$ thick film with superior resistivity and inferior thermopower to a $\text{Na}_{0.5}\text{CoO}_2$ bulk showed a comparable power factor with a $\text{Na}_{0.5}\text{CoO}_2$ bulk.

Author Contributions: A.T., M.M., and I.T. conceived and designed the experiments; A.T. and M.T. performed the experiments; A.T., M.M., Y.K., and I.T. analyzed the data; Y.K., Y.M., and W.S. helped with the experiments and discussed the results; A.T. wrote the paper. All authors have read and agreed to the published version of the manuscript.

Funding: This work was financially supported by the Future Pioneering Program, “Thermal Management Materials and Technology”, and commissioned by the New Energy and Industrial Technology Development Organization (NEDO) of Japan.

Conflicts of Interest: The authors declare no conflict of interest.

References

1. Shigetomi, S.; Mori, S. Electrical properties of Bi_2Te_3 . *J. Phys. Soc. Jpn.* **1956**, *11*, 915–919. [[CrossRef](#)]
2. Satterthwaite, C.B.; Ure, R.W., Jr. Electrical and thermal properties of Bi_2Te_3 . *Phys. Rev.* **1957**, *108*, 1164. [[CrossRef](#)]
3. Lin, W.P.; Wesolowski, D.E.; Lee, C.C. Barrier/bonding layers on bismuth telluride (Bi_2Te_3) for high temperature thermoelectric modules. *J. Mater. Sci. Mater. Electron.* **2011**, *22*, 1313–1320. [[CrossRef](#)]
4. Zhao, L.D.; Lo, S.H.; Zhang, Y.; Sun, H.; Tan, G.; Uher, C.; Wolverton, C.; Dravid, V.P.; Kanatzidis, M.G. Ultralow thermal conductivity and high thermoelectric figure of merit in SnSe crystals. *Nature* **2014**, *508*, 373–377. [[CrossRef](#)] [[PubMed](#)]

5. Zhao, L.D.; Tan, G.; Hao, S.; He, J.; Pei, Y.; Chi, H.; Wang, H.; Gong, S.; Xu, H.; Dravid, V.P.; et al. Ultrahigh power factor and thermoelectric performance in hole-doped single-crystal SnSe. *Science* **2016**, *351*, 141–144. [[CrossRef](#)]
6. Nishino, Y. Electronic structure and transport properties of pseudogap system Fe₂VAl. *Mater. Trans.* **2001**, *42*, 902–910. [[CrossRef](#)]
7. Mikami, M.; Kobayashi, K.; Kawada, T.; Kubo, K.; Uchiyama, N. Development of a thermoelectric module using the heusler alloy Fe₂VAl. *J. Electron. Mater.* **2009**, *38*, 1121–1126. [[CrossRef](#)]
8. Fu, C.; Bai, S.; Liu, Y.; Tang, Y.; Chen, L.; Zhao, X.; Zhu, T. Realizing high figure of merit in heavy-band p-type half-Heusler thermoelectric materials. *Nat. Commun.* **2015**, *6*, 8144. [[CrossRef](#)]
9. Nan, K.; Kang, S.D.; Li, K.; Yu, K.J.; Zhu, F.; Wang, J.; Dunn, A.C.; Zhou, C.; Xie, Z.; Agne, M.T.; et al. Compliant and stretchable thermoelectric coils for energy harvesting in miniature flexible devices. *Sci. Adv.* **2018**, *4*, 5849. [[CrossRef](#)]
10. Zhang, B.; Sun, J.; Katz, H.E.; Fang, F.; Opila, R.L. Promising thermoelectric properties of commercial PEDOT: PSS materials and their Bi₂Te₃ powder composites. *ACS Appl. Mater. Interfaces* **2010**, *2*, 3170–3178. [[CrossRef](#)]
11. Sato, M.; Takeda, M. Fabrication and evaluation of a flexible thermoelectric device using metal thin films. Presented at the ICT 2005 24th International Conference on Thermoelectrics, Clemson, SC, USA, 24 October 2005; pp. 175–178. [[CrossRef](#)]
12. Iwasaki, Y.; Takeda, M. Development of flexible thermoelectric device: Improvement of device performance. In Proceedings of the 2006 25th International Conference on Thermoelectrics, Vienna, Austria, 6–10 August 2006; pp. 562–565. [[CrossRef](#)]
13. Ney, L.; Tepner, S.; Wengenmeyr, N.; Linse, M.; Loren, A.; Bechmann, S.; Weber, R.; Pospischil, M.; Clement, F. Optimization of fine line screen printing using in-depth screen mesh analysis. *AIP Conf. Proc.* **2019**, *2156*, 020006. [[CrossRef](#)]
14. Zeng, P.; Tian, B.; Tian, Q.; Yao, W.; Li, M.; Wang, H.; Feng, Y.; Liu, L.; Wu, W. Screen-printed, low-cost, and patterned flexible heater based on ag fractal dendrites for human wearable application. *Adv. Mater. Technol.* **2019**, *4*, 1800453. [[CrossRef](#)]
15. Tepner, S.; Wengenmeyr, N.; Ney, L.; Linse, M.; Pospischil, M.; Clement, F. Improving wall slip behavior of silver pastes on screen emulsions for fine line screen printing. *Sol. Energ. Mater. Sol. Cells* **2019**, *200*, 109969. [[CrossRef](#)]
16. He, P.; Cao, J.; Ding, H.; Liu, C.; Neilson, J.; Li, Z.; Kinloch, I.A.; Derby, B. Screen-printing of a highly conductive graphene ink for flexible printed electronics. *ACS Appl. Mater. Interfaces* **2019**, *11*, 32225–32234. [[CrossRef](#)]
17. Hatala, M.; Gemeiner, P.; Hvojník, M.; Mikula, M. The effect of the ink composition on the performance of carbon-based conductive screen printing inks. *J. Mater. Sci. Mater. Electron.* **2019**, *30*, 1034–1044. [[CrossRef](#)]
18. Varghese, T.; Hollar, C.; Richardson, J.; Kempf, N.; Han, C.; Gamarachchi, P.; Estrada, D.; Mehta, R.J.; Zhang, Y. High-performance and flexible thermoelectric films by screen printing solution-processed nanoplate crystals. *Sci. Rep.* **2016**, *6*, 33135. [[CrossRef](#)]
19. Feng, J.; Zhu, W.; Deng, Y.; Song, Q.; Zhang, G. Enhanced antioxidation and thermoelectric properties of the flexible screen-printed Bi₂Te₃ films through interface modification. *ACS Appl. Energy Mater.* **2019**, *2*, 2828–2836. [[CrossRef](#)]
20. Terasaki, I.; Sasago, Y.; Uchinokura, K. Large thermoelectric power in NaCo₂O₄ single crystals. *Phys. Rev. B* **1997**, *56*, R12685. [[CrossRef](#)]
21. Caillat, T.; Carle, M.; Pierrat, P.; Scherrer, H.; Scherrer, S. Thermoelectric properties of (Bi_xSb_{1-x})₂Te₃ single crystal solid solutions grown by the T.H.M. method. *J. Phys. Chem. Solids* **1992**, *53*, 1121–1129. [[CrossRef](#)]
22. Park, K.; Jang, K.U.; Kwon, H.-C.; Kim, J.-G.; Chod, W.-S. Influence of partial substitution of Cu for Co on the thermoelectric properties of NaCo₂O₄. *J. Alloy Compd.* **2006**, *419*, 213–219. [[CrossRef](#)]
23. Shu, G.J.; Prodi, A.; Chu, S.Y.; Lee, Y.S.; Sheu, H.S.; Chou, F.C. Searching for stable Na-ordered phases in single-crystal samples of γ -Na_xCoO₂. *Phys. Rev. B* **2007**, *76*, 184115. [[CrossRef](#)]
24. Terasaki, I.; Tsukada, I.; Iguchi, Y. Impurity-induced transition and impurity-enhanced thermopower in the thermoelectric oxide NaCo_{2-x}Cu_xO₄. *Phys. Rev. B* **2002**, *65*, 195106. [[CrossRef](#)]
25. Mikami, M.; Yoshimura, M.; Mori, Y.; Sasaki, T.; Funahashi, R.; Matsubara, I. Crystal growth of thermoelectric material Na_xCoO_{2-δ} by a flux method. *Jpn. J. Appl. Phys.* **2002**, *41*, L777–L779. [[CrossRef](#)]

26. Shin, W.; Izu, N.; Matsubara, I.; Murayama, N. Thermoelectric properties of sinter-forged NaCo_2O_4 . *Jpn. J. Appl. Phys.* **2003**, *42*, 7013–7017. [[CrossRef](#)]
27. Tsuruta, A.; Nomura, K.; Mikami, M.; Kinemuchi, Y.; Terasaki, I.; Murayama, N.; Shin, W. Unusually small thermal expansion of ordered perovskite oxide $\text{CaCu}_3\text{Ru}_4\text{O}_{12}$ with high conductivity. *Materials* **2018**, *11*, 1650. [[CrossRef](#)]
28. Tsuruta, A.; Itoh, T.; Mikami, M.; Kinemuchi, Y.; Terasaki, I.; Murayama, N.; Shin, W. Trial of an all-ceramic SnO_2 gas sensor equipped with $\text{CaCu}_3\text{Ru}_4\text{O}_{12}$ heater and electrode. *Materials* **2018**, *11*, 981. [[CrossRef](#)]
29. Terasaki, I.; Ishii, Y.; Tanaka, D.; Takahata, K.; Iguchi, Y. Thermoelectric properties of $\text{NaCo}_{2-x}\text{Cu}_x\text{O}_4$ improved by the substitution of Cu for Co. *Jpn. J. Appl. Phys.* **2001**, *40*, L65–L67. [[CrossRef](#)]
30. Tajima, S.; Tani, T.; Isobe, S.; Koumoto, K. Thermoelectric properties of highly textured NaCo_2O_4 ceramics processed by the reactive templated grain growth (RTGG) method. *Mater. Sci. Eng. B* **2001**, *86*, 20–25. [[CrossRef](#)]
31. Lee, M.; Viciu, L.; Li, L.; Wang, Y.; Foo, M.L.; Watauchi, S.; Pascal, R.A., Jr.; Cave, R.J.; Ong, N.P. Large enhancement of the thermopower in Na_xCoO_2 at high Na doping. *Nat. Mater.* **2006**, *5*, 537–540. [[CrossRef](#)]
32. Heikes, R.R.; Ure, R.W. *Thermoelectricity: Science and Engineering*; Interscience Publishers: New York, NY, USA, 1961.
33. Koshibae, W.; Maekawa, S. Effects of spin and orbital degeneracy on the thermopower of strongly correlated systems. *Phys. Rev. Lett.* **2001**, *87*, 236603. [[CrossRef](#)]
34. Koshibae, W.; Tsutsui, K.; Maekawa, S. Thermopower in cobalt oxides. *Phys. Rev. B* **2000**, *62*, 6869. [[CrossRef](#)]



© 2020 by the authors. Licensee MDPI, Basel, Switzerland. This article is an open access article distributed under the terms and conditions of the Creative Commons Attribution (CC BY) license (<http://creativecommons.org/licenses/by/4.0/>).